Journal of Materials Chemistry C

ROYAL SOCIETY OF CHEMISTRY

PAPER

View Article Online
View Journal | View Issue

Check for updates

Cite this: J. Mater. Chem. C, 2025, 13, 16024

VS_4–NiAl LDH composite electrodes for next-generation high-performance supercapacitors†

Rajesh Katru,[a] Rakshita Muddamalla,[a] Kamakshaiah Charyulu Devarayapalli,[b] Haranath Divi,[a] Rakesh Kumar Rajaboina,[a] Uday Kumar Khanapuram *[a] and Dae Sung Lee *[b]

Received 22nd March 2025,
Accepted 14th June 2025

DOI: 10.1039/d5tc01244a

rsc.li/materials-c

Transition metal dichalcogenides (TMDs), particularly vanadium tetrasulfide (VS_4), have demonstrated potential for versatile applications in photochemical, electrochemical, energy harvesting, and energy storage applications over a period of time owing to their unique structural and redox properties. In this study, VS_4 was integrated with nickel aluminium layered double hydroxide (LDH) at varying concentrations (2.5 wt%, 5 wt%, and 7.5 wt%) *via* a hydrothermal approach to enhance its capacitive performance. Among the composites, VS_4 + LDH(5%) exhibited superior electrochemical characteristics with a high specific capacitance of 740 F g^{-1} at 0.4 A g^{-1} in 3 M KOH. Furthermore, a symmetric supercapacitor device fabricated using this composition delivered an energy density of 6.65 W h kg^{-1}, yielding a suitable power density of 598.5 W kg^{-1} at a current density of 1 A g^{-1} applied within an operating potential window of 1.2 V. For the validation of the practical application of the SC device, we powered small electronic devices, underscoring the potential of VS_4 + LDH composites as an active and viable electrode material for advanced supercapacitors, bridging the gap between novel material designs and real-world applications.

Open Access Article. Published on 17 June 2025. Downloaded on 3/25/2026 12:38:58 AM.
This article is licensed under a Creative Commons Attribution-NonCommercial 3.0 Unported Licence.

1. Introduction

Fossil fuel-based technologies are increasingly being phased out in favour of more sustainable alternatives as their detrimental influence on human health and the environment becomes ever more apparent. The emergence of new energy sources and storage solutions driven by remarkable recent technological progress has gained paramount importance in addressing these challenges.[1,2] In particular, energy storage devices (ESDs) have become extremely catalytic in overcoming these challenges by enhancing the technologies of renewable energy sources and maximizing grid integration.[3] Some of the challenges that ESDs face today are high production costs and inconsistent reproducibility, which pose substantial impediments to their commercialization.[4,5] Therefore, recent research has focused on developing high-performance ESDs with enhanced power density and increased energy density using novel materials with unique structures for commercial producibility.[6,7]

Supercapacitors (SCs), also known as ultracapacitors or electrochemical capacitors, take the lead in the energy storage industry, presenting unique features that set them apart from other energy-storage systems and provide a distinct advantage.[8] They are widely recognized for their environmental friendliness, high power density, rapid charge–discharge capability, safety, and long cycle life.[9–12] Based on their energy storage mechanisms, SCs are classified as pseudocapacitors, electric double-layer capacitors (EDLCs), and hybrid supercapacitors.[13–15] EDLCs' charge storage process is defined by ion adsorption and desorption at the electrode–electrolyte interface, as opposed to pseudocapacitors', which rely on surface-driven ion or proton insertion and extraction. In the case of hybrid SCs, the mechanism combines pseudocapacitive ion insertion/extraction and electrical double-layer capacitance, enabling enhanced energy storage capabilities.[16,17] Among the various components, the electrode material plays a pivotal role in determining the performance characteristics of an SC. A well-designed, optimized electrode material can significantly enhance the energy storage capacity, power density, and cycle life of SCs.

In this context, two-dimensional (2D) materials have received a great deal of attention as SC electrode materials in recent years.[18–20] As next-generation candidates for electrochemical energy storage devices, 2D materials offer several notable advantages: (i) the surface area is expanded in 2D nanosheets owing to the exposure of surface atoms; (ii) the edge sites of 2D nanosheets exhibit

[a] Department of Physics, Energy Materials and Devices (EMD) Lab, National Institute of Technology, Warangal-506004, India. E-mail: kanapuram.udaykumar@nitw.ac.in
[b] Department of Environmental Engineering, Kyungpook National University, Buk-gu, Daegu 41566, Republic of Korea. E-mail: daesung@knu.ac.kr

† Electronic supplementary information (ESI) available. See DOI: https://doi.org/10.1039/d5tc01244a

This journal is © The Royal Society of Chemistry 2025

Open Access Article. Published on 17 June 2025. Downloaded on 3/25/2026 12:38:58 AM. This article is licensed under a Creative Commons Attribution-NonCommercial 3.0 Unported Licence.

enhanced chemical reactivity, while the open van der Waals gaps facilitate electrolyte ion intercalation; and (iii) they possess exceptional mechanical strength and flexibility at the atomic scale.[21,22] Among these layered materials, transition metal-based compounds have emerged as particularly attractive for developing high-performance energy storage devices. A major competitor in the post-graphene era is the 2D transition metal dichalcogenide (TMD). Its huge surface area and varied oxidation states make it suitable for both faradaic and EDLC storage methods.[23,24]

Various types of layered materials, especially TMDs, are currently employed in SC applications. Among these materials, vanadium disulfide (VS_2) features a 2D layered structure, with vanadium atoms snuggled between two layers of sulfur held together by weak van der Waals forces.[23,25] This structure has been extensively studied for energy storage applications due to its favorable properties, including an interlayer spacing of 5.76 Å that facilitates efficient ion and electron transport.[26,27] Furthermore, vanadium tetrasulfide (VS_4) in its monoclinic form has a narrow band gap of 1.0 eV, allowing for comparatively strong electronic conductivity. The structural arrangement of VS_4, with an interchain spacing of 5.83 Å, creates an abundance of active sites that promote efficient ion diffusion and storage. The sulfur atoms in VS_4 exist as S_2^{2-} and are attached to the adjacent vanadium (V) atoms.[28] Consequently, VS_4 can be characterized as $V^{4+}(S_2^{2-})_2$, and due to its chain-like structure, this material enables rapid electrolyte ion transport, enhancing its reaction kinetics.[29] Moreover, VS_4's higher sulfur content plays a key role in electrochemical reactions in enhanced ionic intercalation and, therefore, has superior reaction capacity to VS_2.[30] Its remarkable properties have made it a go-to electrode material for SC and lithium-ion battery manufacturers, fuelling its widespread commercial deployment as well.[31,32] However, despite its promises, pristine VS_4 faces limitations due to poor rate capability and cycling stability, stemming from inadequate electron conductivity and significant volume changes during cycling.[33–35] To address these issues, researchers have devised various strategies to boost the reaction kinetics and structural integrity.[36]

Composite materials, incorporating carbon nanotubes (CNTs), graphenes, and layered double hydroxides (LDHs), have been developed to amplify the properties of VS_4 and unlock its full potential. LDHs stand out among metal oxide/hydroxide materials as prospective electrodes for high-performance SCs. Their exclusive combination of high redox activity, cost-effectiveness, and environmental sustainability surpasses that of CNTs and graphenes, making LDHs attractive alternatives.[37] Moreover, their distinct sheet-like architecture facilitates rapid ion transport, enhances ion exchange flexibility, and allows for tailored composition.[38] LDHs feature a versatile, brucite-like host structure comprising tunable and oxidizable metal elements. This framework is interspersed with guest spaces containing interlayer anions and water molecules, enabling dynamic interactions and modifications.[39] LDHs, in general, can be explained with the following formula: $[M_{1-x}^{2+}M_x^{3+}(OH)_2](A^{n-})_{x/n}\cdot mH_2O$, where M^{2+} indicates a divalent cation (*e.g.*, Zn^{2+}, Co^{2+}, Mg^{2+}, Cu^{2+}, and Ni^{2+}), M^{3+} indicates a trivalent cation (including Cr^{3+}, Mn^{3+}, Fe^{3+}, and Al^{3+}), and A^{n-} stands for the interlayer exchangeable anions (such as SO^{4-}, OH^-, and NO^{3-}).[40–42]

In this study, we synthesized a VS_4 + NiAl LDH composite featuring a flower flake-like morphology composed of nanolayers *via* a rapid hydrothermal method. The composite capitalizes on its layered architecture to achieve a high surface area, enhancing the electrochemical activity. The VS_4 + NiAl LDH composite electrode delivers an outstanding electrochemical property, characterized by a specific capacitance of 740 F g^{-1} at 0.4 A g^{-1}, which significantly exceeds that of pure vanadium sulfide, demonstrating an excellent electrochemical performance for a 3-electrode set up with 3 M KOH as the aqueous electrolyte at a voltage window starting from 0 to 0.6 V. Furthermore, a symmetric flat cell was assembled using the VS_4 + NiAl LDH(5%) composite, which delivered an impressive energy density of 6.65 W h kg^{-1} and a corresponding power density of 598.5 W kg^{-1} at a current density of 1 A g^{-1}. Furthermore, we evaluated the composite electrode's cycling stability over 2500 cycles, observing 86.95% retention capacity after 1500 cycles at 1 A g^{-1}. These results indeed highlight the potential of VS_4 in NiAl LDH composites with its high cyclability and cost-effectiveness for sustainable energy storage solutions. The fabricated symmetric supercapacitor in the form of a coin cell demonstrated its practical application by powering a watch and calculator for 200–250 seconds and a set of 3 LEDs for several seconds, showcasing its potential as a reliable and efficient energy storage solution.

2. Experimental

2.1. Materials

The analytical grade chemicals were used to synthesize VS_4 and VS_4 + NiAl LDH without any additional purification. Nickel(II) nitrate hexahydrate ($Ni(NO_3)_2\cdot 6H_2O$), aluminum nitrate nonahydrate ($Al(NO_3)_3\cdot 9H_2O$), urea ($CO(NH_2)_2$), ammonium fluoride (NH_4F), ammonium metavanadate (NH_4VO_3), thioacetamide (TAA), potassium hydroxide (KOH), carbon black (super C_{65}), and polyvinylidene fluoride (PVDF) were procured from Sisco Research Laboratories Pvt. Ltd (SRL). Double-distilled water (DI water), *N*-methyl-2-pyrrolidone (NMP) (C_5H_9NO), and ethanol (C_2H_6O) were used to prepare a homogeneous solution.

2.2. Preparation of VS_4

The anemone-like VS_4 was synthesized by a solvothermal method as shown in step 1 of Fig. 1. NH_4VO_3 (85.5 mmol) and CH_3CSNH_2 (4 mmol) taken in a stoichiometric ratio were dissolved in 20 mL of NMP, helped by heating at 70 °C and held under magnetic stirring for 30 minutes for homogenous mixing of the precursors. Then, 20 mL of ethanol was added to the above solution with continuous stirring at 30 °C for 1 h. The mixture was then moved to a 100 mL autoclave lined with Teflon and heated to 160 °C for 24 h in an oven. The solid precipitate from the autoclave was collected by centrifugation at 8000 rpm and then repeatedly washed with water and ethanol. Ultimately, the precipitate was vacuum dried at

Open Access Article. Published on 17 June 2025. Downloaded on 3/25/2026 12:38:58 AM. This article is licensed under a Creative Commons Attribution-NonCommercial 3.0 Unported Licence.

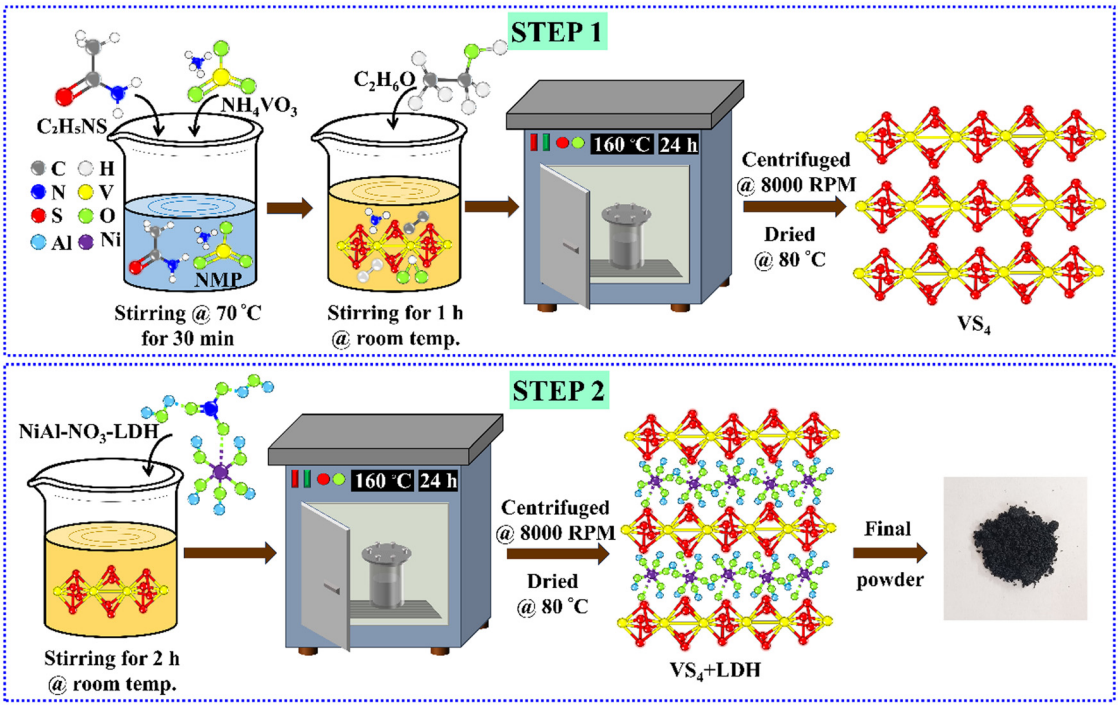

Fig. 1 Schematic of the hydrothermal synthesis of VS_4 and VS_4 + LDH composite material.

80 °C overnight. The solvents were used to increase the interatomic distance for better electrochemical performance of the metals used.[43] The following chemical equation represents the synthesis process:

$$2NH_4VO_3 + 8C_2H_5NS \rightarrow 2VS_4 + 4NH_3 + 13CO_2 + 10H_2O + 3C_2H_6O \quad (1)$$

2.3. Preparation of the NiAl LDH

The NiAl LDH compound was prepared by a hydrothermal method. $Ni(NO_3)_2{\cdot}6H_2O$ (3 mmol) and $Al(NO_3)_3{\cdot}9H_2O$ (1 mmol) were dissolved in 100 mL of DI water and kept under magnetic stirring till a homogeneous solution was formed. To the prepared solution, $CO(NH_2)_2$ (2 mmol) and NH_4F (8 mmol) were added and kept under magnetic stirring for 1 h. The mixture was then placed in a 250 mL Teflon-lined autoclave and heated at 140 °C for 20 h. The precipitate was separated by centrifugation, washed sequentially with deionized water and ethanol, and dried at 60 °C for 12 h to obtain the NiAl LDH compound.

2.4. Preparation of the VS_4 + NiAl LDH composite

The VS_4 + NiAl LDH composites were synthesized by a rapid solvothermal process; the schematic representation is shown in step 2 of Fig. 1. The stoichiometric ratio of C_2H_5NS and NH_4VO_3 dissolution was achieved by treating the materials with 20 mL of NMP by stirring magnetically at 70 °C for 30 minutes. Subsequently, 20 mL of ethanol was added, and the solution was stirred at 30 °C for 1 h. Subsequently, concentration mass ratios of 2.5%, 5%, and 7.5% of the as-prepared LDH powder were added to the mixture for three different solutions and stirred at room temperature for 2 h. The mixture was then transferred to a 100 mL Teflon-lined autoclave and hydrothermally treated at 160 °C for 24 h. The obtained black powder was recovered by centrifugation, rinsed with DI water and ethanol sequentially, and dried at 80 °C for 12 h to obtain the VS_4 + NiAl LDH composite.

2.5. Material characterization details

The morphology of the VS_4 + LDH composite materials was studied by field emission scanning electron microscopy (FESEM) (JEOL-JST-IT800) and high-resolution transmission electron microscopy (HR-TEM) (Fei TECNAI T20). To analyze the elemental composition and quantify the atomic and weight percentages of the constituent elements, energy-dispersive X-ray spectroscopy (EDX) was performed in conjunction with FESEM. Phase identification and crystallinity were assessed by powder X-ray diffraction (PXRD) measurements, conducted over a 2θ range of 10° to 80° using an Anton Paar diffractometer (model: XRDYNAMIC500). Raman spectra were acquired using a RAMAN 785 ER instrument to identify vibrational modes. Fourier transform infrared (FTIR) spectroscopy was conducted in the spectral range of 400–4000 cm^{-1} with a resolution of 4 cm^{-1} using a PerkinElmer spectrophotometer (model: 100S). The samples were prepared by a potassium bromide (KBr) pellet technique. Additionally, high-resolution X-ray photoelectron spectroscopy (XPS) was performed using a Thermo Scientific K-Alpha system to analyze the surface elemental composition and determine the oxidation states of the elements present in the composite.

 This journal is © The Royal Society of Chemistry 2025

Open Access Article. Published on 17 June 2025. Downloaded on 3/25/2026 12:38:58 AM.
This article is licensed under a Creative Commons Attribution-NonCommercial 3.0 Unported Licence.

2.6. Fabrication of Ni foam/VS_4 electrodes and electrochemical tests

Initially, the nickel foam (NF) substrate was thoroughly cleaned by sonication in 3 M HCl for 30 minutes to remove impurities. Following this, it was thoroughly rinsed with deionized water and ethanol until a neutral pH was achieved. The cleaned NF was then kept in an oven at 60 °C overnight for drying and weighed using a high-precision micro-digit balance before further processing. For the efficient transport of ions and for the optimization of the reaction environment, the design of the electrode is very crucial.[44] Therefore, the working electrode was constructed by adding VS_4, carbon black, and PVDF in a mass ratio of 8/1/1, and the resulting mixture was homogenized with 1–2 mL of NMP. Usually, the capacitance of the materials depends on the thickness of the coating, which increases with the increase in the mass loading.[45] Therefore, the slurry was slowly coated optimally onto a nickel foam by a drop-casting method with the help of a micro pipette in an area of 1 cm^2 and was then heated at 80 °C overnight to vaporise the organic solvent. The same procedure was followed even for the VS_4 + LDH(x) (x = 2.5%, 5%, and 7.5%) composite electrodes. The composite mixtures contain between 1.2 and 1.4 mg of VS_4 or VS_4 + LDH(x) as the electroactive material. Electrochemical characterization was performed using an ORIGALYS electrochemical workstation (OGF-500). The evaluations included cyclic voltammetry (CV), galvanostatic charge–discharge (GCD), and electrochemical impedance spectroscopy (EIS) using a 3 M KOH aqueous solution as the electrolyte. The platinum rod and Ag/AgCl were used as the counter and reference electrodes, respectively.

3. Results and discussion

3.1. Morphological analysis

The morphology of VS_4 and its composite NiAl-LDH was extensively characterized by FESEM, TEM, and HRTEM, as shown in Fig. 2. These techniques provided valuable insights into the structural evolution and interface interactions between VS_4 and the LDH. VS_4 standalone of the FESEM revealed an intriguing anemone-like structure, comprising nanorods as shown in Fig. 2(a). This unique morphology suggests a high surface area and has potential for efficient electrochemical reactions. Upon the incorporation of NiAl + LDH(5%), the VS_4 structure underwent significant transformations, resulting in a nano–flower-flake type morphology shown in Fig. 2(b) and (c). However, as shown in Fig. S1 (ESI†), the 2.5% and 7.5% LDH concentrations lack the nanoflower-like structure, resulting in poorer electrochemical performance. Therefore, the overall flower-like hierarchical structure of VS_4 + LDH(5%) is beneficial for uses such as supercapacitors and batteries because of its inherent porosity. EDX analysis of the VS_4 + LDH(5%) composite confirms the presence of V, S, Ni, Al, and O elements, with their corresponding atomic and weight percentages presented in Fig. 2(d). TEM analysis reveals VS_4 + LDH(5%) nanoflakes with diameters of several tens of nanometers, as shown in Fig. 2(e). Further structural information obtained from HRTEM and SAED analyses is presented in Fig. 2(f) and (g) of the VS_4 + LDH(5%) composite. The SAED concentric ring patterns specify the Bragg reflection planes with their interplanar spacing of 0.57 nm for the VS_4 + LDH(5%) composite sample, as compared to the value of 0.56 for VS_4,[46] respectively. It shows clear lattice fringes, increased interlayer spacing when compared to VS_4, and homogeneous nanoflake distribution, facilitating ion/electron transfer and improving electrochemical kinetics.

3.2. Structural analysis

To determine the crystalline phase of VS_4 and VS_4 + LDH(x) (x = 2.5%, 5%, and 7.5%) composites, XRD analysis was performed, as shown in Fig. 3(a). The VS_4 + LDH(5%) composite has characteristic peaks at 21.4°, 23.6°, 31°, 35°, 38°, 45.15°,

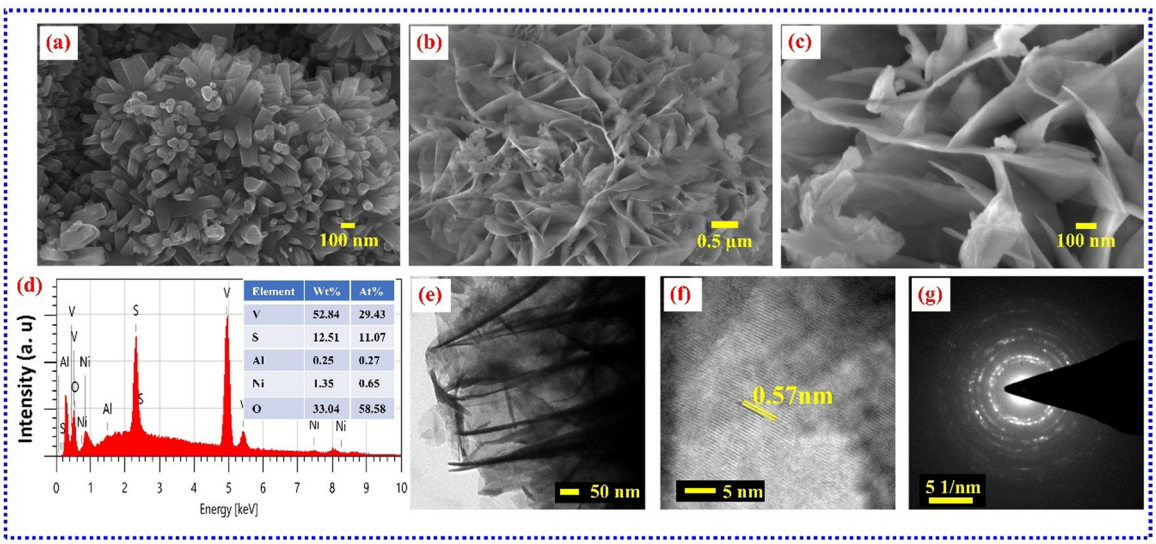

Fig. 2 FESEM images of (a) VS_4 and (b) and (c) VS_4 + LDH(5%) at low and high magnifications. (d) EDX spectra of VS_4 + LDH(5%) (inset shows the atomic and weight percentage). (e) Transmission electron microscopy (TEM) image, (f) high-resolution TEM (HR-TEM) image and (g) SAED pattern of the VS_4 + LDH(5%) composite.

Open Access Article. Published on 17 June 2025. Downloaded on 3/25/2026 12:38:58 AM.
This article is licensed under a Creative Commons Attribution-NonCommercial 3.0 Unported Licence.

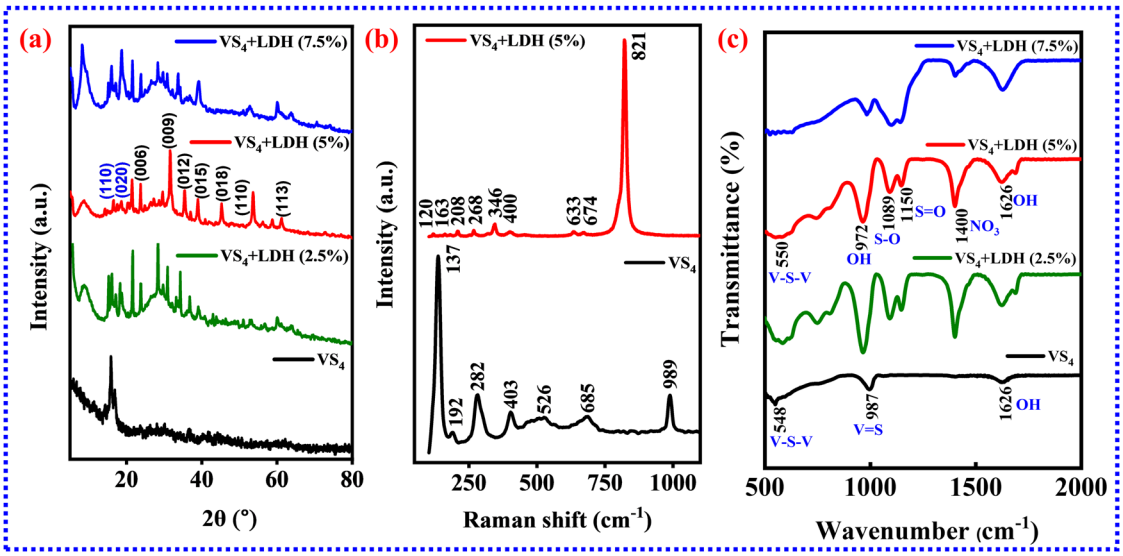

Fig. 3 (a) XRD pattern of VS_4 and VS_4 + LDH(x) (x = 2.5%, 5%, and 7.5%). (b) Raman spectra of VS_4 and VS_4 + LDH(5%). (c) FTIR spectra of VS_4 and VS_4 + LDH(x) (x = 2.5%, 5%, and 7.5%) composites.

and 53.52°, which belong to the (006), (009), (012), (015), (018) (110), and (113) planes of NiAl-LDH (JCPDS no. 15-0087). The planes correspond to the rhombohedral phase of NiAl-LDH.[47] The peaks at 15.93° and 16.92° for VS_4 belong to the (110) and (020) planes, and all observed diffraction peaks are indexed to the monoclinic phase of VS_4 (JCPDS no. 21-1434).[48,49]

Fig. 3(b) illustrates the Raman spectra of the prepared VS_4 and VS_4 + LDH(5%) composite. The two bands located at 137, 282, and 989 cm^{-1} corresponded to the stretching and bending vibrations of the V–S bond, respectively. The peaks at 120, 163, and 346 cm^{-1} correspond to the stretching and bending of the basal and non-basal planes of the NiAl-LDH. The functional groups present, chemical structure, and vibrational modes of the prepared materials were studied by FTIR spectroscopy. The FTIR spectra of VS_4 and VS_4 + LDH(x) (x = 2.5%, 5%, and 7.5%) composites were recorded over the range of 500–2000 cm^{-1}, as illustrated in Fig. 3(c). The absorption peaks occurred at 550, 972, 1089, 1150, 1400, and 1626 cm^{-1} corresponding to VS_4 + LDH(5%). The vibrational modes of VS_4 also cause the expansion of the V–S–V metal ion group, giving rise to smaller peaks at 550 cm^{-1}. The absorption bands at 1089 cm^{-1} and 1150 cm^{-1} correspond to the stretching vibrations of the S–O and S=O bonds, respectively. The broad band at 972 cm^{-1} and a weaker band at 1626 cm^{-1} are assigned to the stretching and bending vibrations of OH-groups from adsorbed water, respectively. The absorption peak at 1400 cm^{-1} indicates the stretching vibration of the N–O bond of NO_3. The FTIR confirms the bonding stretching vibration of the VS_4 and VS_4 + LDH(x) (x = 2.5%, 5%, and 7.5% composites).

XPS was employed to study the composition, valence states, and purity of the synthesized VS_4 + LDH(5%) composite material.[50] Fig. 4(a) shows the VS_4 + LDH(5%) composite material survey spectrum, indicating the presence of primary elements, for instance, vanadium, sulfur, oxygen, nickel, and aluminum, without any impurities. The XPS survey spectrum and the illustration of the corresponding elemental presence of VS_4 + LDH(2.5%) and VS_4 + LDH(7.5%) are illustrated in the ESI† (Fig. S2a and S3a). Fig. 4(b) depicts the binding energy (BE) of V 2p displaying two peaks: the first peak, at 517.51 eV, corresponds to V $2p_{3/2}$, while the second peak, at 524.97 eV, corresponds to V $2p_{1/2}$, respectively. The XPS spectra of VS_4 + LDH(2.5% and 7.5%) (Fig. S2b and S3b, ESI†) revealed shifts in the V 2p peaks. Specifically, the V $2p_{3/2}$ and V $2p_{1/2}$ peaks for V^{4+} occurred at 517.38 eV and 524.11 eV (2.5% LDH), and 516.6 eV and 524.40 eV (7.5% LDH).[51] Fig. 4(c) illustrates the XPS spectra of the S 2p spectra, which confirms the presence of S_2^{2-} dimer peaks at 164.00 eV and 162.84 eV, corresponding to S $2p_{1/2}$ and S $2p_{3/2}$. The XPS spectra of VS_4 + LDH(2.5% and 7.5%) displayed shifts in the S 2p peaks, as illustrated in Fig. S2c and S3c (ESI†). The S $2p_{3/2}$ and S $2p_{1/2}$ peaks were observed at 162.82 eV and 164.18 eV for the 2.5% LDH and at 162.86 eV and 163.96 eV for the 7.5% LDH. This finding implies that the architecture of VS_4 can be adjusted effectively with the layered molecule-level regulation of the LDH structure at the optimised concentration. This observation underscores the superior structural and electrochemical performance of VS_4 + LDH(5%), highlighting its advantages over other composite materials.[52,53] In Fig. 4(c), the obtained VS_4 + LDH(5%) composite displays three characteristic peaks at 532.12 eV, 533.98 eV, and 535.80 eV, which correspond to V–O, defective O, and adsorbed O, respectively. The peak position and peak area ratio of the three types of oxygen species differ from those of the precursor VS_4 and the fully converted product V_2O_3, owing to the unique composition of the heterostructure. The XPS spectra of VS_4 + LDH(2.5% and 7.5%) showed shifts in the O 1s peaks (V–O, defective O, and adsorbed O), as depicted in Fig. S2d and S3d (ESI†). The analysis indicates that extrinsic adsorbed oxygen is crucial in the synthesis method of the VS_4 + LDH composite.[54,55] The VS_4

 This journal is © The Royal Society of Chemistry 2025

Open Access Article. Published on 17 June 2025. Downloaded on 3/25/2026 12:38:58 AM.
This article is licensed under a Creative Commons Attribution-NonCommercial 3.0 Unported Licence.

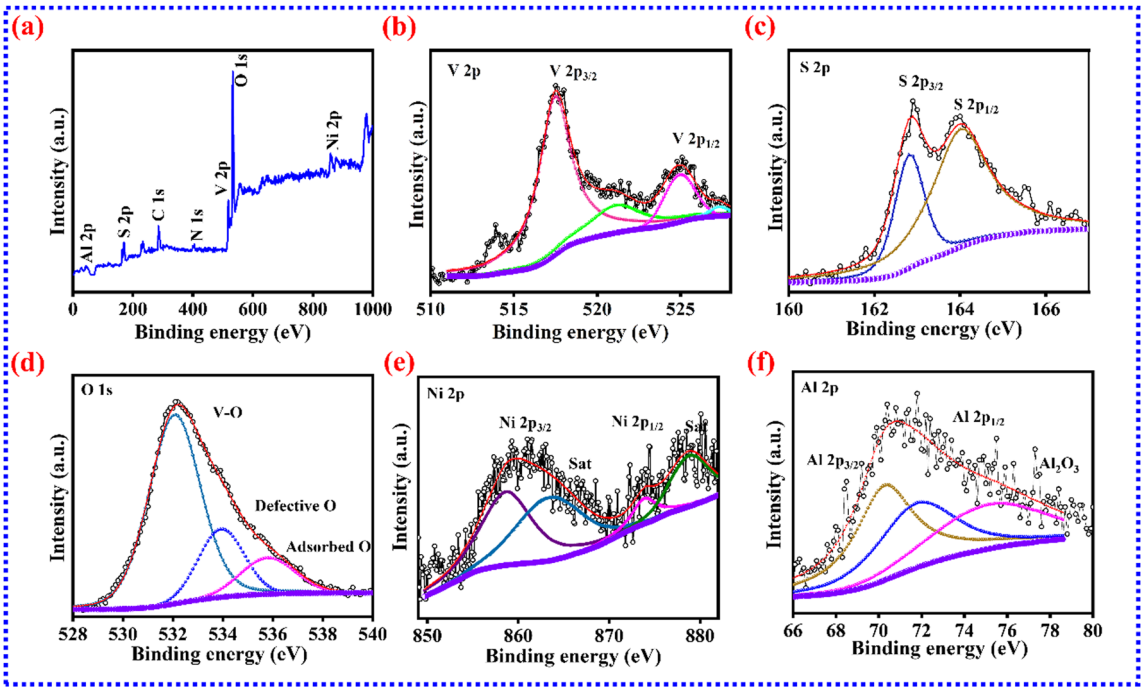

Fig. 4 (a) Wide-range XPS survey spectrum, (b) V 2p, (c) S 2p, (d) O 1s, (e) Ni 2p, and (f) Al 2p of the VS_4 + LDH(5%) composite material.

combination with the LDH has the potential to modify the distribution of surface charge, which may enhance electrostatic charge. This may lead to a significantly favourable change in binding energy. Furthermore, the specific quantities of the LDH added to the composite are 2.5%, 5%, and 7.5%. Consequently, the elements present in the LDH (Ni and Al) exist at very low concentrations, resulting in significantly low peak intensities in the corresponding XPS analysis. The VS_4 combination with the LDH has the potential to modify the distribution of surface charge, which may enhance electrostatic charge. This may lead to a significantly favorable change in binding energy. Furthermore, the specific quantities of the LDH added to the composite are 2.5%, 5%, and 7.5%. Consequently, the elements present in the LDH (Ni and Al) exist at very low concentrations, resulting in significantly low peak intensities of XPS spectra. Fig. 4(e) shows the Ni 2p high-resolution spectra. Around 858.90 eV, it deconvolutes into two peaks, which are identified as the Ni $2p_{3/2}$ and Ni $2p_{1/2}$ orbitals of Ni^{2+} at 855.71 eV, 855.83 eV, which are slightly higher than those of VS_4 + LDH(2.5%) and VS_4 + LDH(7.5%), respectively, as shown in Fig. S2 and S3 (ESI†). The peaks at 863.92 eV and 878.72 eV at VS_4 + LDH(5%) Fig. 4(e), 862.92 eV, and 876.54 eV at VS_4 + LDH(2.5%) (Fig. S2e, ESI†), 862.52 eV, and 878.98 eV at VS_4 + LDH 7.5% (Fig. S3e, ESI†) are supplemental satellite peaks of the Ni $2p_{3/2}$ and Ni $2p_{1/2}$ orbitals. The Al 2p spectra (Fig. 4(f)) shows that the peaks at binding energies of 70.29 eV and 71.94 eV correspond to the Al $2p_{3/2}$ and Al $2p_{1/2}$ orbitals of Al^{3+} in VS_4 + LDH(5%), while the peak at 75.57 eV indicates the presence of Al^{3+} species in $Al(OH)_3$. Furthermore, oxygen displays a peak with a B.E. value of 532.15 eV, which aligns with the metal–oxygen bonds.[56] The peaks at 67.81 eV and 73.40 eV, and at 67.68 eV and 73.48 eV, correspond to the Al $2p_{3/2}$ and Al $2p_{1/2}$ orbitals of VS_4 + LDH (2.5%) and (7.5%) (Fig. S2f and S3f, ESI†), respectively.[57] The shifts in binding energies of V^{4+}, S^{2-}, Ni^{2+}, and Al^{3+} suggest a strong interfacial chemical interaction between VS_4 and the NiAl-LDH, indicating significant electronic coupling between the two components.

3.3. Electrochemical analysis

The electrochemical activity of the as-synthesized VS_4 and VS_4 + LDH(x) (x = 2.5%, 5%, and 7.5%) composite electrodes was investigated by CV, GCD, and EIS measurements using 3 M KOH electrolyte in a three-electrode cell configuration using an electrochemical workstation. The fundamental study of the current associated with the electrode as a function of time concerning the applied potential is interpreted from the CV.[58] The electrochemical behaviour of these electrodes was evaluated by the CV at a scan rate from 5 mV s^{-1} to 100 mV s^{-1} in the potential window of 0 to 0.6 V using a three-electrode apparatus, as shown in Fig. 5(a)–(d). All these electrodes display two prominent redox peaks on the cathodic and anodic curves, corresponding to the continuous oxidation and reduction occurring within the VS_4 and VS_4 + LDH(x) (x = 2.5%, 5%, and 7.5%) composite electrodes. The peaks at 0.33 V, 0.35 V, 0.36 V, and 0.39 V are due to the oxidation of vanadium (V^{3+} to V^{5+}) and high sulfur content in VS_4 and VS_4 + LDH(x) (x = 2.5%, 5%, and 7.5%) composite materials. The cathode scan of the CV curves reveals peaks at 0.20 V, 0.21 V, 0.19 V, and 0.19 V in VS_4 and VS_4 + LDH(x) (x = 2.5%, 5%, and 7.5%) composite materials, corresponding to a reduction of high sulfur content and vanadium (V^{5+} to V^{4+}, and then to V^{3+}). The CV measurement reveals identifiable redox peaks, indicating that the electrode

Open Access Article. Published on 17 June 2025. Downloaded on 3/25/2026 12:38:58 AM.
This article is licensed under a Creative Commons Attribution-NonCommercial 3.0 Unported Licence.

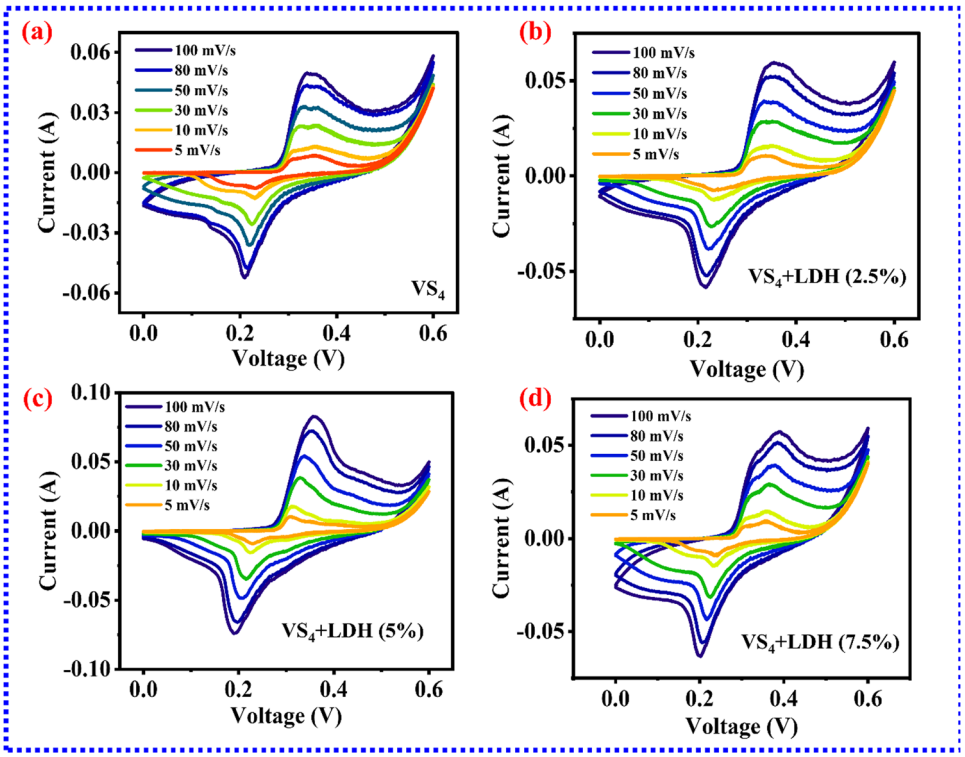

Fig. 5 CV of (a) VS_4, (b) VS_4 + LDH(2.5%), (c) VS_4 + LDH(5%), and (d) VS_4 + LDH(7.5%) composite materials.

material functioned as a faradaic battery and was pseudocapacitive. Even at a higher scan rate, the CV curves stay constant, demonstrating a good rate of capability.

Notably, the VS_4 nanosheets display two broad peaks, characteristic of their faradaic redox behaviour, underscoring their potential for pseudocapacitive energy storage. As the scan rates increase, the cathodic and anodic peaks shift due to the electrode's internal resistance. The rapid electron transfer or redox reactions occur at the electrode–electrolyte interface, facilitating efficient energy storage. Fig. 5(a) shows the CV measurements at different scan rates ranging from 5 to 100 mV s^{-1}. The resulting oxidation and reduction peaks are detected at 0.35 V and 0.23 V at a scan rate of 5 mV s^{-1}, and there is a peak shift as the scan rate is increased. Therefore, the observed peaks at a scan rate of 100 mV s^{-1} were at 0.33 V and 0.20 V, respectively. The VS_4 electrode system exhibits reversible redox reactions, as evidenced by two distinct peaks. This phenomenon is attributed to the synergistic interaction between the electrode and hydroxide ions (OH^-) in the electrolyte. Notably, increasing the scanning speed amplifies the anodic and cathodic peak currents, accompanied by an expansion of the enclosed area. This behavior is indicative of pseudocapacitive characteristics in the electrode. The peak shift is also observed in the VS_4 + LDH(x) (x = 2.5%, 5%, and 7.5%) composite electrodes.

The GCD technique was employed to investigate further the electrochemical properties of VS_4 and VS_4 + LDH(x) (x = 2.5%, 5%, and 7.5%) composite electrodes. All measurements were performed in a 3 M KOH electrolyte within a potential window of 0 to 0.6 V. For the pristine VS_4 electrode, GCD curves were recorded at different current densities ranging from 0.4 A g^{-1} to 3 A g^{-1} to evaluate the rate capability and charge–discharge performance, as shown in Fig. 6(a). Similarly, GCD profiles of the VS_4 + LDH composites with different LDH loadings (2.5%, 5%, and 7.5%) were obtained across the same range of current densities, and are shown in Fig. 6(b)–(d). All GCD curves exhibit a characteristic non-linear behavior, which is a clear indication of pseudocapacitive charge storage mechanisms dominated by faradaic redox reactions involving vanadium ions (V^{5+}/V^{3+}) and the high sulfur content in the structure. As the current density increases, a consistent decrease in discharge time is observed across all samples. This trend is attributed to the limited ion diffusion time at higher current densities, which restricts the full utilization of active sites within the electrode material, thereby reducing the total charge stored during each cycle.

When K^+ and OH^- from the KOH electrolyte interact with VS_4, a chemical reaction occurs. The K^+ ions, being highly electropositive, are attracted to the sulfur atoms in VS_4, leading to the formation of potassium sulfide (K_2S). This reaction involves the transfer of sulfur atoms from the VS_4 lattice to the K^+ ions, resulting in the formation of a new compound. Simultaneously, the OH^- ions from the electrolyte react with the vanadium atoms in VS_4, leading to the formation of vanadium oxyhydroxide ($VO_x(OH)_y$). This reaction involves the incorporation of oxygen and hydrogen atoms from the OH^- ions into the VS_4 lattice, resulting in the formation of a new vanadium-based compound. Overall, the reaction between K^+ and OH^- with VS_4 leads to the formation of new compounds,

 This journal is © The Royal Society of Chemistry 2025

Open Access Article. Published on 17 June 2025. Downloaded on 3/25/2026 12:38:58 AM.
This article is licensed under a Creative Commons Attribution-NonCommercial 3.0 Unported Licence.

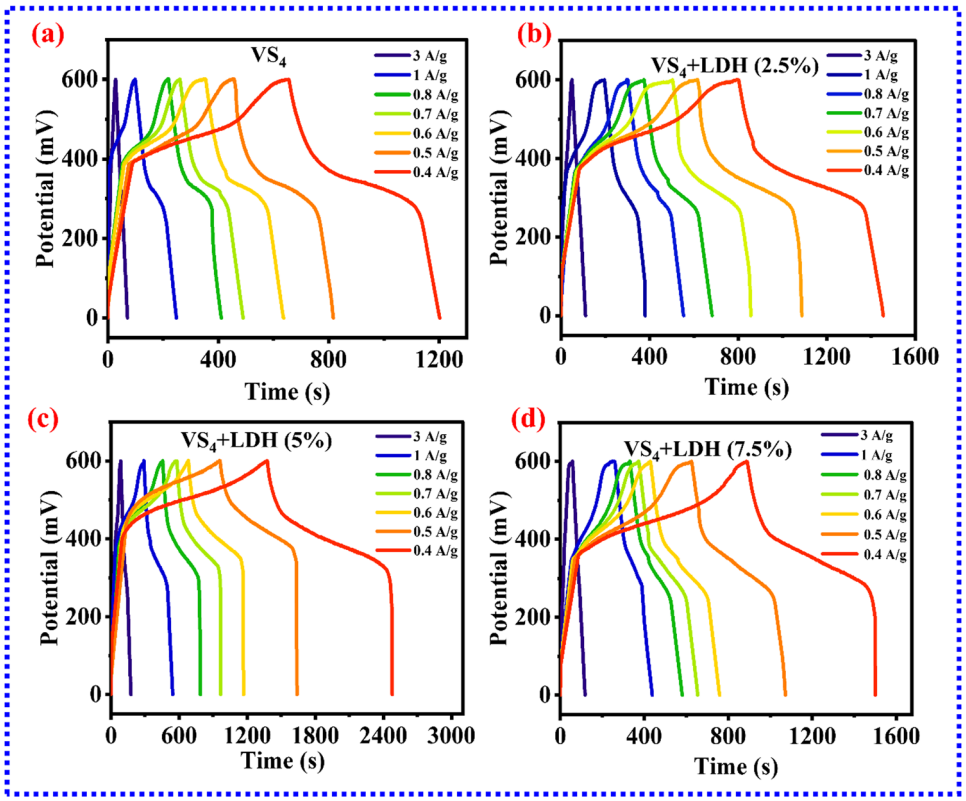

Fig. 6 GCD of (a) VS_4, (b) VS_4 + LDH(2.5%), (c) VS_4 + LDH(5%), and (d) VS_4 + LDH(7.5%) composite materials.

including potassium sulfide and vanadium oxyhydroxide, taking forward the reactivity of the electrochemical kinetics.

The CV comparison of VS_4 and VS_4 + LDH(x) (x = 2.5%, 5%, and 7.5%) composite electrodes at 100 mV s^{-1} scan rate is shown in Fig. 7(a). The electrochemical analysis reveals that the VS_4 + LDH(5%) electrode exhibits the highest specific capacity, surpassing VS_4, VS_4 + LDH(2.5%), and VS_4 + LDH(7.5%), respectively. For comparison, the cyclic voltammetry (CV) curve at 100 mV s^{-1} for the bare Ni foam, which shows negligible activity, is also included in Fig. 7(a). This enhanced performance is attributed to the well-organized arrays and intimate integration of the NiAl-LDH and VS_4, facilitating efficient electron and ion transport and increased surface area in VS_4 + LDH(5%), allowing for greater ion intercalation and specific capacity. CV plots display distinct redox peaks, demonstrating pronounced faradaic reactions in the studied electrodes. The comparative GCD curves at 0.4 A g^{-1} current density of the four electrodes with the 0 to 0.6 V potential window in a 3 M KOH electrolyte solution were constructed. The results show that the VS_4 + LDH(5%) composite material has high specific capacitance when compared to that of VS_4, VS_4 + LDH(2.5%), and VS_4 + LDH(7.5%) materials, as shown in Fig. 7(b). The results reveal that the composite electrode exhibits an extended discharge time, highlighting its outstanding electrochemical performance. Furthermore, it is noted that at elevated current densities, the discharge time decreases due to the impeded diffusion of OH^- ions within the electrode, which somewhat limits its high rate capability. The accelerated discharge at higher currents curtails the intercalation process, resulting in underutilization of the electrode's maximum charge storage potential.[59] The specific capacitance of the electrodes can be calculated from the CV (eqn (2)) and GCD (eqn (3)) curves as follows:[60]

$$C_s = \frac{\int I\mathrm{d}V}{m\nu\Delta V} \quad (2)$$

$$C_s = \frac{I(A)\Delta t}{m\Delta V} \quad (3)$$

where C_s is the specific capacitance, V is the potential, I is the current, m is the mass loading of the material coated on the Ni foam, ν is the scan rate, ΔV is the potential window applied to the electrode, and Δt represents the discharge time.

The capacitance values for the VS_4, VS_4 + LDH(2.5%), VS_4 + LDH(5%), and VS_4 + LDH(7.5%) electrodes at 5 mV s^{-1} scan rate were measured to be 235.53 F g^{-1}, 493.92 F g^{-1}, 874.86 F g^{-1} and 462.36 F g^{-1}, respectively. The capacitance values obtained for the VS_4, VS_4 + LDH(2.5%), VS_4 + LDH(5%), and VS_4 + LDH(7.5%) electrodes were found to be 364 F g^{-1}, 437 F g^{-1}, 740 F g^{-1}, and 405 F g^{-1} at a current density of 0.4 A g^{-1}. The study found that VS_4 + LDH(5%) has a much superior specific capacitance to VS_4, VS_4 + LDH(2.5%), and VS_4 + LDH(7.5%) nanosheets. As shown in Fig. 7(c), the value of C_s decreases with the increase in scan rate, indicating that the proper diffusion of electrolytic ions occurs at a lower scan rate when compared to the higher scan rate. The C_s value of all four electrodes is higher at a lower scan rate (5 mV s^{-1}), owing to the

Open Access Article. Published on 17 June 2025. Downloaded on 3/25/2026 12:38:58 AM.
This article is licensed under a Creative Commons Attribution-NonCommercial 3.0 Unported Licence.

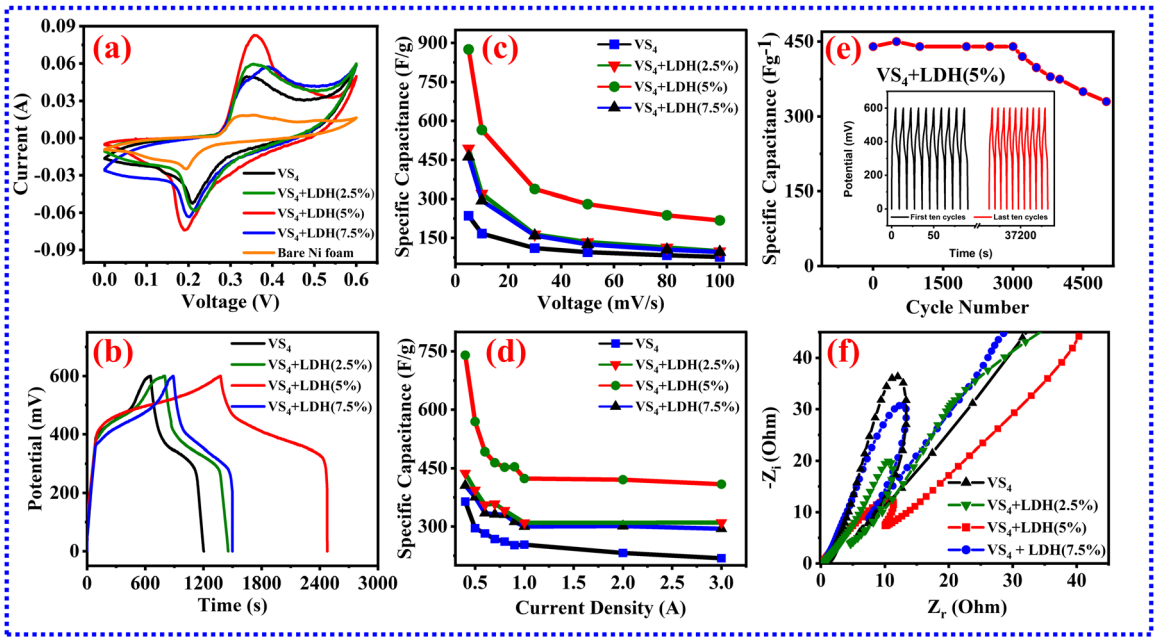

Fig. 7 (a) CV comparison of a bare Ni foam, VS_4 and VS_4 + LDH(x) (x = 2.5%, 5%, and 7.5%) composite electrodes at a 100 mV s^{-1} scan rate. (b) GCD comparison of the four electrodes at 0.4 A g^{-1}, rate capability curve of the four electrodes at (c) different scan rates (5–100 mV s^{-1}) and (d) different current densities (0.4–3 A g^{-1}), and (e) the specific capacitance *vs.* cycle number curve (inset: the initial and the final charge–discharge cycles of consecutive 5000 GCD cycles of the VS_4 + LDH(5%) composite material at 1 A g^{-1}). (f) Nyquist plots of VS_4 and VS_4 + LDH(x) (x = 2.5%, 5%, and 7.5%) composite electrodes.

electrolyte ions diffusing entirely into the electrode and having enough time to flow completely throughout the active area for charge storage. When the scan rate increases, the C_s value of the electrode decreases because of the time limit of the higher scan rates, resulting in the momentum of the electrolyte ions to interpolate the innermost sites of the VS_4 + LDH(5%) composite electrode components in the electrode being limited. Moreover, the overall performance of the electrolyte is very much dependent on the intrinsic molecular properties, and it is increasingly evident that it plays a pivotal role in determining the conductivity and stability of the electrode.[61] This is the reason for the CV curve, with only the outer active surface resulting in charge storage. As a result, the variation identified in the response of the CV and the current performance of the VS_4 + LDH(5%) composite electrode was determined by the ion's physical properties, including the ionic radius, conductivity, ion mobility, and ionic hydration sphere radius, and the K^+ ion ionic radii and hydration number are 1.33 Å and 6.5, which are almost the same as O^{2-} ions, correspondingly. The C_s values of the materials were evaluated not only by the KOH electrolyte's ionic radii for improved diffusion but also by the mobility and conductivity of the ions (K^+ or OH^-). Hereafter, the K^+ ions with a high molar conductivity of 73.5 $cm^2\ \Omega^{-1}\ mol^{-1}$ float on the surface of the electrode/electrolyte to enable improved C_s. The existence of OH^- anions delays the mobility of K^+ cations, which is the primary reason for the fluctuation of capacitance value in VS_4 and VS_4 + LDH(x) (x = 2.5%, 5%, and 7.5%) composite materials.

Fig. 7(d) illustrates the variation in C_s for different current densities for VS_4 and VS_4 + LDH(x) (x = 2.5%, 5%, and 7.5%) composite electrodes using a 3 M KOH electrolyte solution. At a higher charging and discharging rate of 0.4 A g^{-1}, the VS_4 + LDH(5%) electrode retains significantly higher C_s, demonstrating its ability to withstand high charge rates during the intercalation and deintercalation processes. This behaviour underscores the excellent electrochemical stability and robustness of the VS_4 structure under rapid charge–discharge conditions. The observed variability in C_s values derived from CV and GCD measurements arises because CV evaluates capacitance at specific potentials, whereas GCD considers the total potential range and averages the capacitance over this range based on the electrolyte behaviour and sample performance. The averaging of capacitance across the voltage range during GCD analysis can account for the slight differences in C_s. Here, the VS_4 + LDH(5%) nanomaterial exhibits improved capacitive performance due to its unique structure. The proper incorporation of the NiAl LDH into the VS_4 matrix can also be observed from the FESEM and the XPS data. Unlike the morphology of VS_4 + LDH(2.5%) and VS_4 + LDH(7.5%) (Fig. S1, ESI†), the nano-flower flake type morphology of VS_4 + LDH(5%) provides a large surface area, allowing ions to access both surface and core regions, which enables efficient redox reactions. The composite's 2D ultrathin nanosheet structure enables rapid charge transport and provides abundant active sites. The unique horn-like edge arrangement and positively charged LDHs facilitate efficient ion exchange and accessibility, enhancing charge storage. Additionally, sulfur in VS_4 amplifies electrochemical activity, active sites, and electron transport, accelerating the electrochemical kinetics.[62] Moreover, the presence of sulfur in the host VS_4 atoms enhances electrochemical activity, provides additional active

 This journal is © The Royal Society of Chemistry 2025

Open Access Article. Published on 17 June 2025. Downloaded on 3/25/2026 12:38:58 AM.
This article is licensed under a Creative Commons Attribution-NonCommercial 3.0 Unported Licence.

sites, and improves electron transport, ultimately boosting the electrochemical kinetics. These characteristics collectively improve the charge storage and overall electrochemical efficiency of the VS_4 + LDH(5%) electrode. As shown in the FESEM images, the homogeneous distribution of LDH within the VS_4 matrix leads to the formation of a flower-like structure with nanosheets that have an increased surface area and are interconnected in their framework, leading to increased reactivity, and creating a two-dimensional layered structure that facilitates the diffusion of electrolyte ions.

The VS_4 + LDH(5%) composite electrode's long-term cycling stability was tested during 5000 continuous charge and discharge cycles with a specific current of 1 A g^{-1}. Fig. 7(e) depicts the charge and discharge curves for the first and last ten cycles, respectively. After 3500 cycles, the VS_4 + LDH(5%) composite electrodes preserved approximately 90.5% of their initial C_s. As the number of cycles increases, the capacitance retention progressively decreases, and the deterioration process for the electrode begins at 3000 cycles. The cycling stability can be attributed to the following aspects: the interspace within the flower-like VS_4 + LDH(5%) composite helps relieve internal stress caused by volume expansion during electrolyte ion insertion and extraction. This relief mechanism mitigates structural damage, promoting stable cycling performance and enhancing cycle life by reducing internal stress and structural degradation, ultimately enabling more stable charge/discharge processes. Further, the specific capacitance *vs.* cycle number graph shown in Fig. 7(e), we can observe that there is a slight initial increase in capacitance, which can be attributed to the gradual activation of active material within the electrode. As the electrode undergoes repeated charge/discharge cycles, more electrochemically active sites, particularly Ni and V sites, become fully exposed and accessible. This increased exposure enables more efficient charge storage, contributing to the observed capacitance enhancement. As shown in Fig. 7(e), the prolonged cycling, however, leads to capacitance degradation. This decline may be due to structural changes, specifically the transformation of the LDH to β-$Ni(OH)^2$, which occurs during the charge/discharge process.[63] This transformation potentially alters the electrode's electrochemical properties, ultimately affecting its performance. The material's stability declines progressively after 3500 cycles. Pre- and post-cyclic FESEM images are shown in the ESI† for reference (Fig. S4). Therefore, the VS_4 + LDH(5%) composite material crystal structure and shape are largely responsible for its better performance because of its numerous advantages such as high C_s, good rate capability, and reasonable cycling stability. Finally, the VS_4 + LDH(5%) composite electrode promotes effective ion and electron transport and has high C_s at ambient temperature, making it a promising choice for supercapacitor application.

EIS was employed to evaluate the electrical conductivity and charge-transfer characteristics of the electrode materials. The measurements were conducted over a frequency range of 0.01 Hz to 100 kHz with an applied AC amplitude of 10 mV. The resulting Nyquist plot, shown in Fig. 7(f), has a quasi-semicircular shape at high frequencies, where the *x*-intercept represents the material's internal or ohmic resistance (R_s). This resistance encompasses the ionic resistance of the electrolyte, the intrinsic material resistance, and the contact resistance between components. Notably, the diameter of the semicircle on the impedance spectrum indicates the charge-transfer resistance (R_{ct}), providing insights into the material's conductivity, with a smaller diameter indicating higher conductivity. The Warburg resistance (W), reflected by the slope of the low-frequency linear segment, signifies the degree of ion diffusion and electrochemical interaction between the electrode material and the surrounding electrolyte.[64] As shown in Fig. 7(f), VS_4 + LDH(5%) has a lower R_s value (0.33 Ω), representing the slope at low frequency, signifying that the VS_4 + LDH(5%) composite has a lower Warburg resistance (W) and a higher ion diffusion rate.

Given the pseudocapacitive behavior of the VS_4 + LDH(5%) composite electrode, its kinetic characteristics were elucidated by examining the corresponding CV plot. Fig. 8(a)–(f) illustrate the capacitive and diffusion role of the VS_4 + LDH(5%) composite electrode at different scan rates (5 to 100 mV s^{-1}). As the scan rate increases, the diffusive contribution decreases while the surface-controlled capacitive phenomenon rises. This behaviour occurs because, at lower scan rates, electrolyte ions can fully diffuse into the microporous network, whereas at higher scan rates, the charge storage mechanism becomes dominated by surface phenomena. The oxidative and reductive peak currents exhibit a highly linear relationship, with values from the linear regression analysis being very close to 1. The linear regression analysis confirms the diffusion-regulated charge storage behaviour in the VS_4 + LDH(5%) electrode, highlighting the importance of both diffusion-controlled and capacitive processes in governing the electrochemical energy storage.[65,66] Eqn (4) can be used to explain the relationship between peak currents and scan rates.

$$i = a\nu^b \quad (4)$$

where ν is the scan rate, i is the achieved peak current, a is a constant, and b indicates the charge storage mechanism. The capacitance contribution is assessed by plotting log(i) *versus* log(v) of the anodic and cathodic peak current densities (I, A g^{-1}), according to a power-law relationship with scan rate (V, mV s^{-1}). The parameter 'b' is significant, as it represents the combined effects of capacitive electrochemical processes and ionic diffusion. Notably, 'b' values of 1 and 0.5 correspond to ideal capacitive and diffusive behaviors, respectively, in charge storage. Fig. 8(g) shows that the calculated b value of 0.61 for the VS_4 + LDH(5%) electrode suggests a combined mechanism, where both capacitive contributions and ion diffusion-controlled processes play a role. The immediate electrical current can be expressed as the proportion contribution of the capacitive and diffusion behaviour, and it can be determined using eqn (5):[67]

$$i = k_1 v + k_2 v^{1/2} \quad (5)$$

where 'i' is the peak current density and 'v' the scan rate; k_1 and k_2 are constant values. A distinct k_1 value is derived for each

Open Access Article. Published on 17 June 2025. Downloaded on 3/25/2026 12:38:58 AM.
This article is licensed under a Creative Commons Attribution-NonCommercial 3.0 Unported Licence.

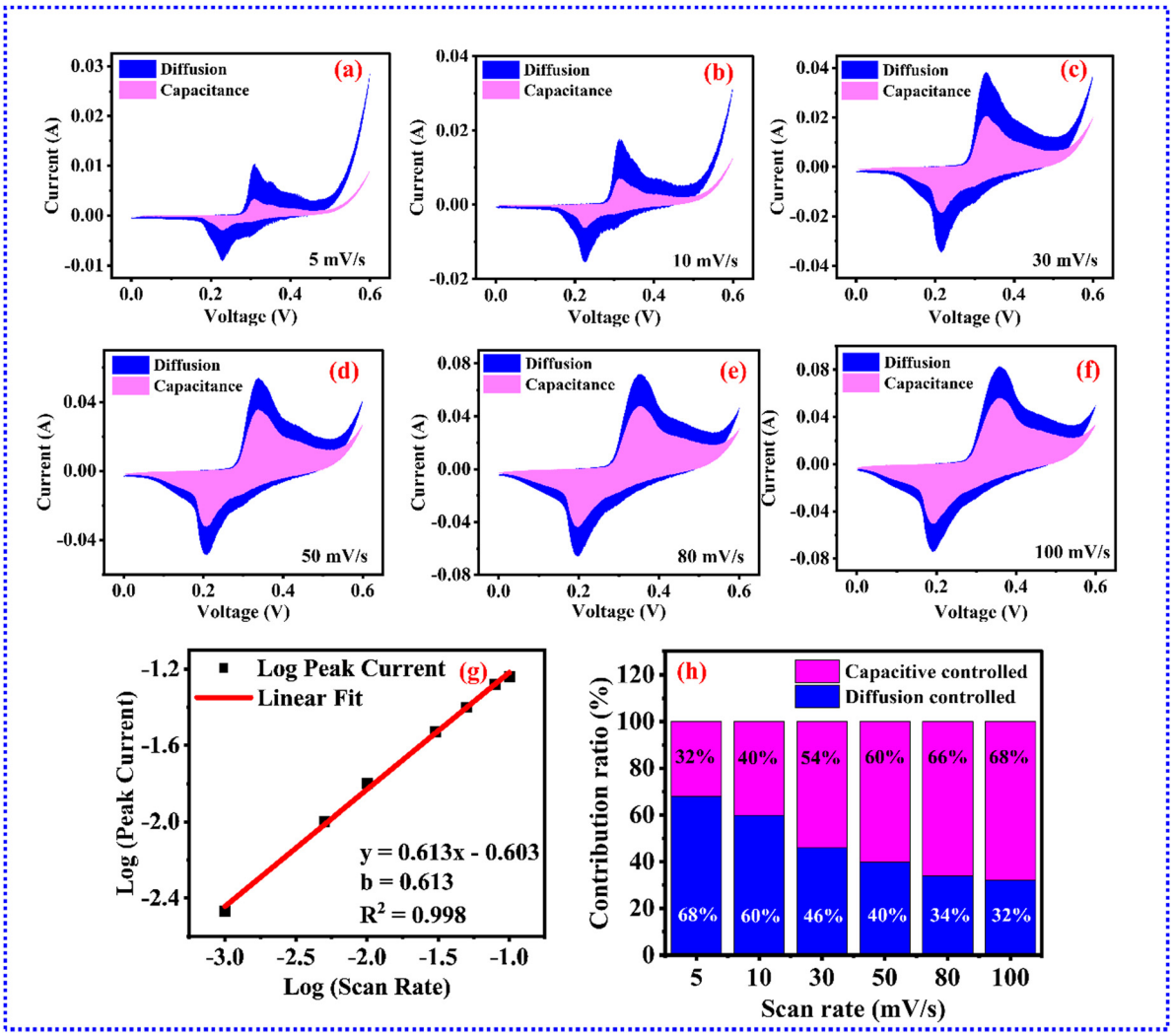

Fig. 8 (a)–(f) CV plots of the VS_4 + LDH(5%) composite material at different scan rates extending from 5 to 100 mV s^{-1} in 3 M KOH with the contribution of diffusion and capacitive controlled surface process. (g) *b* value of the VS_4 + LDH(5%) composite electrode material. (h) Plot illustrating the charge contribution from surface capacitive and diffusive processes as a function of scan rate.

specific voltage through a fitting analysis. Fitting analysis yields a k_1 value for each specific voltage, where k_1v represents the capacitive current contribution and $k_2v^{1/2}$ represents the diffusion-controlled current contribution. By determining k_1 and k_2 at a given potential, the relative contributions of pseudocapacitive and diffusive processes to the overall capacitance can be precisely determined. As shown in Fig. 8(h), the proportion of surface capacitive control in the charge storage process was evaluated at different scan rates of 5, 10, 30, 50, 80, and 100 mV s^{-1} as 32.0%, 40%, 54%, 60%, 66%, and 68%, respectively. The capacitive contribution increases progressively with the scan rate, indicating that the surface redox reaction plays a dominant role in the charge storage mechanism, particularly at high scan rates.

3.4. Device testing and application

To comprehensively analyse and understand the electrochemical performance of the VS_4 + LDH(5%) composite electrodes, a symmetric two-electrode device that serves as both the cathode and the anode was fabricated with 6 M KOH used as the electrolyte solution. The CV of the symmetric cell shows a potential window ranging from −0.6 to 0.6 V at different scan rates from 10 to 40 mV s^{-1}, as shown in Fig. 9(a). The CV profiles exhibit a quasi-rectangular shape at various scan rates, signifying an ideal capacitive behaviour.[68]

The GCD curves of the VS_4 + LDH(5%) composite electrode at different current densities ranging from 0.4 A g^{-1} to 2 A g^{-1} are shown in Fig. 9(b). These curves show mostly pseudocapacitor behaviour, in correspondence with the CV of the sample. The specific capacitance values at different current densities were determined using eqn (6):[69]

$$C_s = \frac{2I(A)\Delta t}{m\Delta V} \text{F g}^{-1} \quad (6)$$

The EIS analysis was performed to evaluate the resistive behaviour of the electrode material and the electrolyte solution

 This journal is © The Royal Society of Chemistry 2025

Open Access Article. Published on 17 June 2025. Downloaded on 3/25/2026 12:38:58 AM.
This article is licensed under a Creative Commons Attribution-NonCommercial 3.0 Unported Licence.

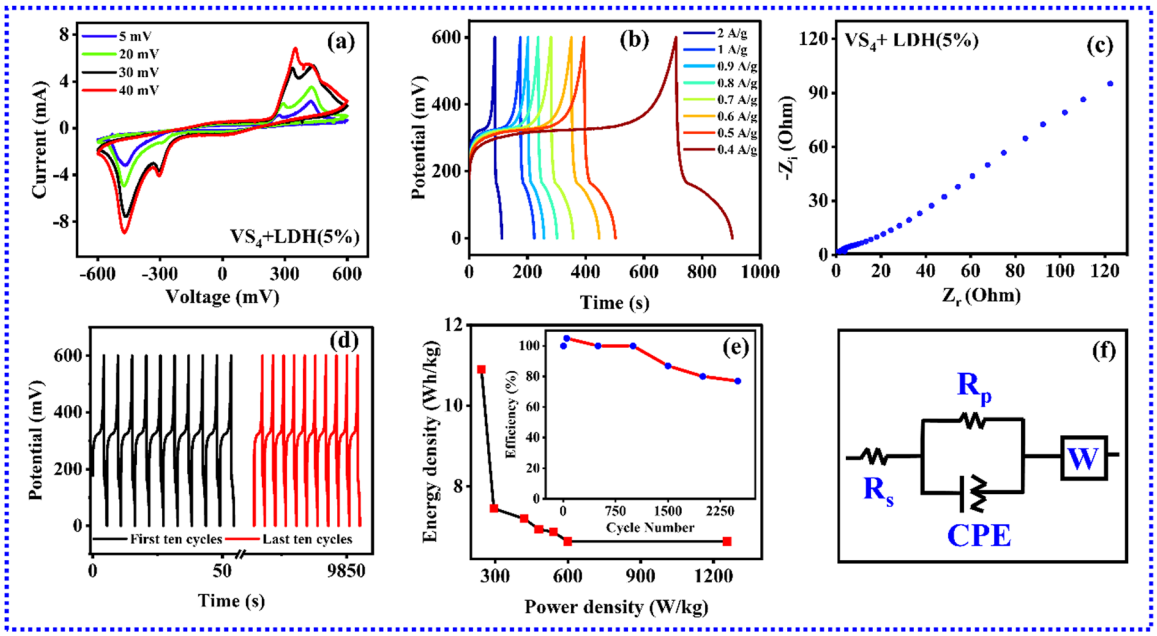

Fig. 9 (a) CV curves, (b) GCD curves, (c) Nyquist plot, (d) stability plot for 2500 cycles, (e) specific energy *versus* specific power profile (Ragone plots) of cells (inset: CS retention of material for 2500 cycles), and (f) circuit diagram.

in supercapacitor applications. The Nyquist plot was obtained from impedance measurements spanning a broad frequency range of 0.01 Hz to 100 kHz, as shown in Fig. 9(c).

A two-electrode system was employed to investigate the cyclic durability of the supercapacitor, a critical parameter for practical uses. As depicted in Fig. 9(d), the stability test results reveal a reasonable cycling stability, with the device maintaining 86.95% of its initial capacity over 2500 cycles at a current density of 1 A g^{-1}. In Fig. 9(e) (inset), the efficiency percentage per cycle for 2500 cycles is also included, and the FESEM image of the post-2500-cycles of the VS_4 + LDH(5%) SC device active electrode material is depicted in Fig. S5 of the ESI.† The reduction in capacitance preservation in the device is caused by the mechanical stress on the electrode during the electrolyte intercalation, which weakens it and hence reduces the electrode stability. Moreover, during the charging–discharging cycles, an activation process occurs, similar to the three-electrode configuration, resulting in an initial increase and a subsequent gradual decline in specific capacity.

The performance metrics of the supercapacitor were evaluated in terms of energy density (E) and power density (P), which are the two important characteristics of supercapacitors. The E and P of the VS_4 + LDH(5%) composite electrodes were calculated and represented in the Ragone plot, as shown in Fig. 9(e). The energy density (E) and power density (P) of the two-electrode system were derived from the specific capacitance according to eqn (7) and (8):[70,71]

$$\text{Energy density}\,(E) = \frac{1}{2}\frac{C_s \times \Delta V^2}{3.6}(\text{W h kg}^{-1}) \qquad (7)$$

$$\text{Power density}\,(P) = \frac{E \times 3600}{\Delta t}\,(\text{W kg}^{-1}) \qquad (8)$$

where ΔV is the voltage window, Δt the discharge time, and C_s the specific capacitance of the cell. The maximum energy density of the device was 6.65 W h kg^{-1}, with a corresponding power density of 598.5 W kg^{-1} at a current density of 1 A g^{-1}. The symmetric device with VS_4 + LDH(5%) electrodes achieves a substantial improvement in energy density, especially at elevated power densities. According to eqn (7), a reasonably high specific capacity and a wide potential window are necessary preconditions for reaching high energy density. The VS_4 + LDH(5%) composite electrode with a high sulfur content, with the inclusion of LDHs at a specific concentration, has a high specific surface area, coupled with the radially grown nanoflake morphology, providing a high density of active sites, resulting in an improved specific capacity.

The equivalent circuit model shown in Fig. 9(f) comprises a resistor, a capacitor, and a constant-phase element (CPE), which collectively simulate the complex electrochemical behavior and reactions occurring within the system. The series resistance (R_s), representing the ohmic drop between the electrode and the electrolyte, was determined to be 1.33 Ω from the intercept with the Z-axis at high frequencies, as shown in Table 1. The fitted Nyquist circuit confirms the predominance of pseudocapacitive behaviour, consistent with the CV and GCD data. These results highlight the excellent electrochemical performance of the VS_4 + LDH(5%) composite electrode-based supercapacitor.

Further, a symmetric supercapacitor device was fabricated for real-world applications, as depicted in Fig. 10(a). The device was assembled using a VS_4 + LDH(5%) composite electrode slurry coated onto two conductive copper sheets, with cellulose paper serving as the separator. The nano VS_4 + LDH(5%) composite electrode slurry was applied to copper sheets

Open Access Article. Published on 17 June 2025. Downloaded on 3/25/2026 12:38:58 AM.
This article is licensed under a Creative Commons Attribution-NonCommercial 3.0 Unported Licence.

Table 1 EIS fitted parameters from the Nyquist plot

Parameters	End values of VS_4 + LDH(5%) device
Series resistance (R_s)	1.33 Ω
Constant-phase element CPE	Y_0 = 0.00761, n = 0.69
Charge transfer resistance (R_{p_1})	48.6 Ω
Warburg impedance (W)	0.00853

through the doctor blade method and subsequently dried in a vacuum oven at 70 °C for 12 h. To complete the assembly, a few drops of 6 M KOH electrolyte solution were added to the separator arrangement. Further, the conductive sheets, spacer, and spring were packed into a coin cell. The fabricated symmetric cells were placed in a coin cell holder, as shown in the inset of Fig. 10(a), to prevent air exposure and evaporation during testing. The SC device was fabricated and connected to the resistance–capacitance (RC) circuit to form a combined energy storage system. Their charging and discharging behaviours were analysed using an RC circuit, as illustrated in Fig. 10(b). The devices were charged with a constant voltage supply for 30 seconds, after which the power source was disconnected. The charged supercapacitor-powered devices, such as a watch and a calculator, are shown in Fig. 10(c) and (d), respectively. The charged supercapacitor successfully powered the watch and calculator for 200 to 250 seconds (see ESI,† Videos S1 and S2) and a set of 3 LEDs for a few seconds. This practical demonstration highlights the potential of VS_4 + LDH(5%) composite material-based supercapacitors for energy storage and portable applications. For the comparison study, we include some of the recent works conducted on VS_4 and its composites in Table 2.

4. Conclusions

A series of VS_4 + NiAl LDH nanocomposites with different weight percentages of NiAl LDH(2.5%, 5%, and 7.5%) were successfully synthesized *via* a facile solvothermal method. The incorporation of the NiAl LDH into the VS_4 matrix resulted in a significant enhancement of supercapacitor performance,

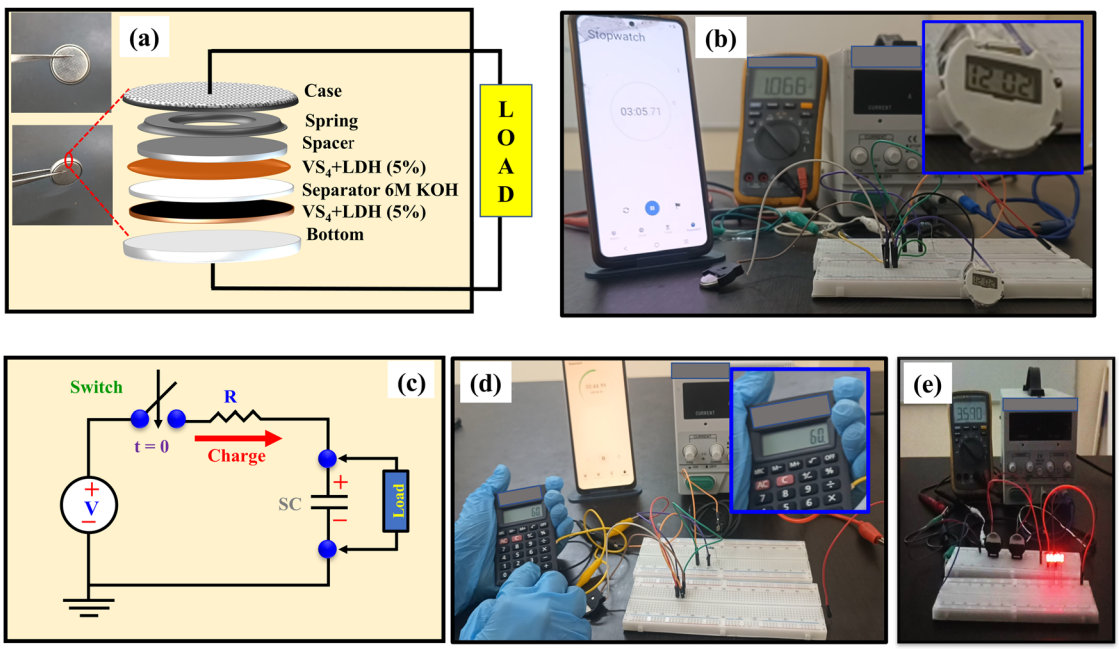

Fig. 10 (a) Schematic of the fabrication of the coin cell (inset: fabricated coin cell). (b) Reference RC circuit for electrical connections. Illumination of (c) a watch, (d) a calculator, and (e) a 5-LED device powered by an SC.

Table 2 Comparative study of VS_4 and its composites

S. no.	Electrode material	Synthesis method	Specific capacitance (F g^{-1})	Scan rate/current density (A g^{-1})	Cycling stability	Ref.
1	VS_4/CNT	Hydrothermal	330	1	51% after 5000 cycles	72
2	VS_4-CC@VS_3	Hydrothermal	206	1	93% after 1000 cycles	73
3	VS_4/rGO	Hydrothermal	877	0.5	90% after 1000 cycles	74
4	VS_4/Sb	Hydrothermal	539.4	3	174% after 10 000 cycles	75
5	VS_4/MXene	Solvothermal	332.1	1	88.5% after 10 000	76
6	VS_4	Solvothermal	617	0.4	93.8% after 12 000 cycles	77
7	VS_4 + NiAl LDH	Solvothermal	740	0.4	90.5% after 3500	This Work

 This journal is © The Royal Society of Chemistry 2025

Open Access Article. Published on 17 June 2025. Downloaded on 3/25/2026 12:38:58 AM.
This article is licensed under a Creative Commons Attribution-NonCommercial 3.0 Unported Licence.

demonstrating the potential of these nanocomposites for advanced energy storage applications. The optimised incorporation of the LDH into VS_4 led to enhanced performance, as evidenced by the improved specific capacitance values of the fabricated SCs. Among the composites, the VS_4 + LDH(5%) electrode exhibited the most promising electrochemical performance. The exceptional performance of the VS_4 + LDH(5%) composite, as evidenced by the FESEM data, can be attributed to its unique two-dimensional flower-like nanoflake morphology, which offers a high surface area for ion access, and to the presence of electronegative sulfur species that enhance electron transport and redox kinetics. The characterization techniques, especially XPS spectroscopic analysis, confirmed the formation of strong chemical bonds between VS_4 and the NiAl-LDH, resulting in enhanced electrochemical performance of VS_4. The interfacial interaction between VS_4 and the LDH, along with the crucial role of the oxidation states of metal and sulfur ions, facilitates rapid charge transfer kinetics and improved capacitive behavior. Moreover, GCD analysis revealed a high specific capacitance of 740 F g^{-1} at a current density of 0.4 A g^{-1}. Furthermore, a symmetric supercapacitor device fabricated using the VS_4 + LDH(5%) composite achieved a maximum power density of 598.5 W kg^{-1} and an energy density of 6.65 W h kg^{-1}. These features collectively contribute to improved charge storage and transport dynamics, making the material highly suitable for next-generation electrochemical energy storage systems. The VS_4 composite, particularly with 2D materials, shows promise for enhancing the electrochemical performance and scalability. Besides energy storage devices, this composite material has potential applications in photocatalysts, biosensors, solar cells, and drug delivery systems, offering opportunities for future research and development. The electrochemical performance and cycling life of the VS_4 compound can still be improved by doping with other heteroatoms such as boron, phosphorus, nitrogen, oxygen, and fluorine, offering promising directions for future research and development.

Conflicts of interest

The authors declare that they have no known competing financial interests or personal relationships that could have appeared to influence the work reported in this paper.

Data availability

The data that support the findings of this study are available from the corresponding authors upon reasonable request.

Acknowledgements

Authors MR and DH are grateful to the Council of Scientific & Industrial Research (CSIR) and Department of Science and Technology (DST), Government of India, for providing financial support under the projects CSIR – SRF #09/0922(11518)/2021-EMR-I and #CRG/2021/007142, respectively. KCD and DSL acknowledge the research supported by the Basic Science Research Program through the National Research Foundation of Korea (NRF), funded by the Ministry of Education (RS-2018-NR031057). The authors also acknowledge the support of Prof. Manohar Kakunuri, Department of Chemical Engineering, NIT Warangal, and his research scholar, Mr Vikas Mahendra Sharma, with device fabrication and testing.

References

1 A. González, E. Goikolea, J. A. Barrena and R. Mysyk, *Renewable Sustainable Energy Rev.*, 2016, **58**, 1189–1206.
2 L. Gao, M. Cao, C. Zhang, J. Li, X. Zhu, X. Guo and Z. Toktarbay, *Adv. Compos. Hybrid Mater.*, 2024, **7**, 144.
3 H. Gao and B. Wang, *APL Mater.*, 2024, **12**, 091117.
4 Y. Tian, Y. Cai, Y. Chen, M. Jia, H. Hu, W. Xie, D. Li, H. Song, S. Guo and X. Zhang, *Adv. Funct. Mater.*, 2024, **34**, 2316342.
5 X. Chen, S. Wei, J. Wang, F. Tong, T. Söhnel, G. I. N. Waterhouse, W. Zhang, J. Kennedy and M. P. Taylor, *Intermetallics*, 2024, **169**, 108306.
6 D. Cai, Z. Yang, R. Tong, H. Huang, C. Zhang and Y. Xia, *Small*, 2024, **20**, 2305778.
7 H. Sun, A. G. Ebadi, M. Toughani, S. A. Nowdeh, A. Naderipour and A. Abdullah, *Energy*, 2022, **238**, 121555.
8 J. Pu, X. Wang, T. Zhang, S. Li, J. Liu and K. Komvopoulos, *Nanotechnology*, 2015, **27**, 045701.
9 Z. Fan, J. Yan, T. Wei, L. Zhi, G. Ning, T. Li and F. Wei, *Adv. Funct. Mater.*, 2011, **21**, 2366–2375.
10 X. Dai, Y. Dai, J. Lu, L. Pu, W. Wang, J. Jin, F. Ma and N. Tie, *Ionics*, 2020, **26**, 2501–2511.
11 G. Chen, Y. Yang, Y. Dai and W. Wang, *Int. J. Electrochem. Sci.*, 2020, **15**, 5342–5351.
12 J. Gong, Y. Wang, J. Wang, Y. Liu, C. Hu, T. Zhou, Q. Yu, J. Yang and Y. Dai, *Int. J. Hydrogen Energy*, 2022, **47**, 10056–10068.
13 F. He, Z. Hu, K. Liu, S. Zhang, H. Liu and S. Sang, *J. Power Sources*, 2014, **267**, 188–196.
14 H. Wang, Q. Gao and J. Hu, *J. Power Sources*, 2010, **195**, 3017–3024.
15 M. Liu, L. Gan, W. Xiong, Z. Xu, D. Zhu and L. Chen, *J. Mater. Chem. A*, 2014, **2**, 2555–2562.
16 M. Vijayakumar, A. Bharathi Sankar, D. Sri Rohita, T. N. Rao and M. Karthik, *ACS Sustainable Chem. Eng.*, 2019, **7**, 17175–17185.
17 Y. Huang, Y. Huang, M. Zhu, W. Meng, Z. Pei, C. Liu, H. Hu and C. Zhi, *ACS Nano*, 2015, **9**, 6242–6251.
18 H. H. Hegazy, J. Khan, N. Shakeel, E. A. Alabdullkarem, M. I. Saleem, H. Alrobei and I. S. Yahia, *RSC Adv.*, 2024, **14**, 32958–32977.
19 S. A. Kadam, K. P. Kadam and N. R. Pradhan, *J. Mater. Chem. A*, 2024, **12**, 17992–18046.

Open Access Article. Published on 17 June 2025. Downloaded on 3/25/2026 12:38:58 AM. This article is licensed under a Creative Commons Attribution-NonCommercial 3.0 Unported Licence.

20 S. Liu, H. Zhang, X. Peng, J. Chen, L. Kang, X. Yin, Y. Yusuke and B. Ding, *ACS Nano*, 2025, **19**, 13591–13636.
21 H. H. Hegazy, J. Khan, N. Shakeel, E. A. Alabdullkarem, M. I. Saleem, H. Alrobei and I. S. Yahia, *RSC Adv.*, 2024, **14**, 32958–32977.
22 S. Huo, H. Qu, F. Meng, Z. Zhang, Z. Yang, S. Zhang, X. Hu and E. Wu, *Nano Lett.*, 2024, **24**, 11937–11943.
23 K. S. Kumar, N. Choudhary, Y. Jung and J. Thomas, *ACS Energy Lett.*, 2018, **3**, 482–495.
24 X. Liu, J. Shang, J. Li, H. Liu, F. Zhang, Q. Pan and Y. Tang, *Angew. Chem., Int. Ed.*, 2025, **64**, e202420160.
25 R. Sun, Q. Wei, J. Sheng, C. Shi, Q. An, S. Liu and L. Mai, *Nano Energy*, 2017, **35**, 396–404.
26 M. N. Rantho, M. J. Madito, F. O. Ochai-Ejeh and N. Manyala, *Electrochim. Acta*, 2018, **260**, 11–23.
27 X. Wang, Y. Zhang, J. Zheng, H. Jiang, X. Dong, X. Liu and C. Meng, *J. Colloid Interface Sci.*, 2020, **574**, 312–323.
28 R. Sun, Q. Wei, Q. Li, W. Luo, Q. An, J. Sheng, D. Wang, W. Chen and L. Mai, *ACS Appl. Mater. Interfaces*, 2015, **7**, 20902–20908.
29 Y. Zhou, Y. Li, J. Yang, J. Tian, H. Xu, J. Yang and W. Fan, *ACS Appl. Mater. Interfaces*, 2016, **8**, 18797–18805.
30 G. Yang, B. Zhang, J. Feng, H. Wang, M. Ma, K. Huang, J. Liu, S. Madhavi, Z. Shen and Y. Huang, *ACS Appl. Mater. Interfaces*, 2018, **10**, 14727–14734.
31 Y. Zhang, G. Xu, Q. Kang, L. Zhan, W. Tang, Y. Yu, K. Shen, H. Wang, X. Chu, J. Wang, S. Zhao, Y. Wang, L. Ling and S. Yang, *J. Mater. Chem. A*, 2019, **7**, 16812–16820.
32 S. Wang, W. Ma, X. Zang, L. Ma, L. Tang, J. Guo, Q. Liu and X. Zhang, *ChemSusChem*, 2020, **13**, 1637–1644.
33 L. Wang, L. Xue, J. Wang, L. Miao, W. Chen, M. Wan, W. Gong, Q. Liu, N. Zhang and W. Zhang, *J. Alloys Compd.*, 2018, **768**, 938–943.
34 G. Yang, H. Wang, B. Zhang, S. Foo, M. Ma, X. Cao, J. Liu, S. Ni, M. Srinivasan and Y. Huang, *Nanoscale*, 2019, **11**, 9556–9562.
35 X. Wang, Y. Zhang, J. Zheng, X. Liu and C. Meng, *J. Colloid Interface Sci.*, 2019, **554**, 191–201.
36 L. Song, Y. Tang, R. Mao, J. Sun, C. Yu, Y. Liu and Y. Zhao, *ACS Appl. Nano Mater.*, 2024, **7**, 9002–9011.
37 Y. Lin, X. Xie, X. Wang, B. Zhang, C. Li, H. Wang and L. Wang, *Electrochim. Acta*, 2017, **246**, 406–414.
38 J. Cao, Z. Feng, H. Liang, X. Lu and W. Wang, *Chem. Eng. J.*, 2023, **472**, 144872.
39 F. Parsapour, M. Pooriraj, M. Moradi, V. Safarifard and S. Hajati, *Synth. Met.*, 2023, **292**, 117234.
40 Z. P. Diao, Y. X. Zhang, X. D. Hao and Z. Q. Wen, *Ceram. Int.*, 2014, **40**, 2115–2120.
41 F. Lai, Y.-E. Miao, L. Zuo, H. Lu, Y. Huang and T. Liu, *Small*, 2016, **12**, 3235–3244.
42 L. Li, J. Fu, K. S. Hui, K. N. Hui and Y.-R. Cho, *J. Mater. Sci.: Mater. Electron.*, 2018, **29**, 17493–17502.
43 H. Wang, P. Wang, W. Gan, L. Ci, D. Li and Q. Yuan, *J. Power Sources*, 2022, **534**, 231412.
44 X. Li, S. Xiong, G. Li, S. Xiao, C. Zhang and Y. Ma, *Mater. Lett.*, 2023, **346**, 134481.
45 N. Yang, H. Li, X. Lin, S. Georgiadou, L. Hong, Z. Wang, F. He, Z. Qi and W.-F. Lin, *J. Energy Chem.*, 2025, **105**, 669–701.
46 X. Wang, Y. Zhang, J. Zheng, H. Jiang, X. Dong, X. Liu and C. Meng, *J. Colloid Interface Sci.*, 2020, **574**, 312–323.
47 J. Xu, S. Gai, F. He, N. Niu, P. Gao, Y. Chen and P. Yang, *J. Mater. Chem. A*, 2014, **2**, 1022–1031.
48 Z. Li, B. P. Vinayan, P. Jankowski, C. Njel, A. Roy, T. Vegge, J. Maibach, J. M. G. Lastra, M. Fichtner and Z. Zhao-Karger, *Angew. Chem., Int. Ed.*, 2020, **59**, 11483–11490.
49 L. Cao, B. Luo, B. Xu, J. Zhang, C. Wang, Z. Xiao, S. Li, Y. Li, B. Zhang, G. Zou, H. Hou, X. Ou and X. Ji, *Adv. Funct. Mater.*, 2021, **31**, 1–12.
50 T. Zeng, L. Meng, L. Cheng, R. Wang, Z. Ran, D. Liu, J. Fu, J. He, Q. Zhou, Q. Li, Q. Li and C. Yuan, *Adv. Funct. Mater.*, 2025, **35**, 2419278.
51 R. K. Chava, T. Kim, Y. Kim and M. Kang, *J. Mater. Chem. C*, 2023, **11**, 1782–1790.
52 J. Shan, Y. Liu, Y. Su, P. Liu, X. Zhuang, D. Wu, F. Zhang and X. Feng, *J. Mater. Chem. A*, 2016, **4**, 314–320.
53 Y. Liu, R. Huang, N. Wei and Y. Zhou, *Ionics*, 2023, **29**, 651–660.
54 J. Cai, Y. Zhang, Y. Qian, C. Shan and B. Pan, *Sci. Rep.*, 2018, **8**, 11741.
55 G. Maharana, R. Muniramaiah, J. Yuvashree, D. Mandal, S. Mondal, M. Kovendhan, J. M. Fernandes, G. Laxminarayana and D. P. Joseph, *Surf. Interfaces*, 2023, **42**, 103413.
56 C. Ragumoorthy, N. Nataraj, S.-M. Chen and S. Tharuman, *J. Electrochem. Soc.*, 2023, **170**, 117515.
57 F. Hu, E. Cui, H. Liu, J. Wu, Y. Dai and G. Yu, *J. Mater. Sci.: Mater. Electron.*, 2019, **30**, 2572–2584.
58 T. Priyadharshini, M. Lakshmi Narayana, N. K. Murugasenapathi, T. Palanisamy and A. V. Ravindra, *Electrochim. Acta*, 2025, **509**, 145343.
59 Y. Liu, S. P. Jiang and Z. Shao, *Mater. Today Adv.*, 2020, **7**, 100072.
60 H.-Y. Li, J.-K. Feng, L. Xiang, J. Huang and B. Xie, *J. Power Sources*, 2020, **457**, 228031.
61 Y. Zhan, X. Ren, S. Zhao and Z. Guo, *J. Power Sources*, 2025, **629**, 235992.
62 F. B. M. Ahmed, D. Khalafallah, M. Zhi and Z. Hong, *Adv. Compos. Hybrid Mater.*, 2022, **5**, 2500–2514.
63 S. Shen, W. Guo, W. Zhuang, W. Yang, L. Qin, X. Liu and Z. Yue, *J. Phys.: Conf. Ser.*, 2021, **2009**, 012008.
64 A. Sandeep, P. T and A. V. Ravindra, *Mater. Res. Bull.*, 2024, **179**, 112991.
65 S. Ghosh, H. R. Inta, M. Chakraborty, G. Tudu, H. V. S. R. M. Koppisetti, K. S. Paliwal, D. Saha and V. Mahalingam, *ACS Appl. Nano Mater.*, 2022, **5**, 7246–7258.
66 M. Shaheen, M. Z. Iqbal, M. W. Khan, S. Siddique, S. Aftab and S. M. Wabaidur, *Energy Fuels*, 2023, **37**, 4000–4009.
67 S. Chinnasamy and A. Mani, *J. Alloys Compd.*, 2024, **1002**, 175266.
68 X. Song, X. Ma, Y. Li, L. Ding and R. Jiang, *Appl. Surf. Sci.*, 2019, **487**, 189–197.
69 H.-Y. Li, K. Jiao, L. Wang, C. Wei, X. Li and B. Xie, *J. Mater. Chem. A*, 2014, **2**, 18806–18815.

 This journal is © The Royal Society of Chemistry 2025

Open Access Article. Published on 17 June 2025. Downloaded on 3/25/2026 12:38:58 AM.
This article is licensed under a Creative Commons Attribution-NonCommercial 3.0 Unported Licence.

70 T. M. Masikhwa, F. Barzegar, J. K. Dangbegnon, A. Bello, M. J. Madito, D. Momodu and N. Manyala, *RSC Adv.*, 2016, **6**, 38990–39000.
71 W.-J. Youe, S. J. Kim, S.-M. Lee, S.-J. Chun, J. Kang and Y. S. Kim, *Int. J. Biol. Macromol.*, 2018, **112**, 943–950.
72 X. Wang, Y. Zhang, J. Zheng, X. Liu and C. Meng, *J. Colloid Interface Sci.*, 2019, **554**, 191–201.
73 M. Ramu, J. R. Chellan, N. Goli, P. Joaquim, V. Cristobal and B. C. Kim, *Adv. Funct. Mater.*, 2020, **30**, 1906586.
74 S. Ratha, S. R. Marri, N. A. Lanzillo, S. Moshkalev, S. K. Nayak, J. N. Behera and C. S. Rout, *J. Mater. Chem. A*, 2015, **3**, 18874–18881.
75 S. Singal, A. Joshi, G. Singh and R. K. Sharma, *J. Power Sources*, 2020, **475**, 228669.
76 Y. Niu, P. Luo, X. Chen, J. Song, X. He, H. Sun, Z. Li, C. Wang and J. Jiang, *Chem. Eng. J.*, 2024, **493**, 152372.
77 H. Y. Li, J. K. Feng, L. Xiang, J. Huang and B. Xie, *J. Power Sources*, 2020, **457**, 228031.